임의의 방향으로 틀어진 벽면과의 안정적인 접촉을 보장하는 모션/힘 추종 비행 매니퓰레이터 제어

Stable Contact Guaranteeing Motion/Force Control for an Aerial Manipulator on an Arbitrarily Tilted Surface

초록

비행 매니퓰레이터는 멀티로터 형태의 드론에 로봇팔과 같은 매니퓰레이터를 장착한 새로운 형태의 비행체이다. 이 연구에서는 비행 매니퓰레이터에 장착된 엔드이펙터를 통해 임의의 방향으로 틀어진 벽면 상에서 시간에 따라 변하는 위치 및 힘 프로파일을 추종하도록 하는 제어기를 설계한다. 이를 위해 우선 엔드이펙터에 작용하는 힘을 Kelvin-Voigt linear model을 통해 표현한 병진 운동 방정식을 유도하고, 엔드이펙터와 벽면 사이의 안정적인 접촉을 보장하도록 하는 안정성 조건을 토대로 제어기에 사용할 제어 이득 값을 실시간으로 계획하는 알고리즘을 설계하여 외란 추정기 기반의 제어법칙에 적용한다. 또한, 다양한 접근 속도나 힘 프로파일을 적용한 실험을 진행하여 제안한 제어기의 성능을 검증하였다.

Key Words : Unmanned Aerial Manipulation, Motion/Force Control, Perturbed Switched System

Introduction

Remote-controlled or autonomous robots had been utilized for conducting tasks operated in hard-to-reach areas such as disaster recovery sites, radioactively contaminated regions and the middle of a dense forest. Heretofore, a ground-based mobile robot shown in Figure 1(a) had normally been utilized to conduct such tasks. However, there exist several places that are difficult to reach with the ground-based robots.

Figure 1 (a) A ground-based mobile robot and (b) an aerial manipulator

Numerous tall buildings located in the city center need periodical operations such as cleaning, painting, structure-intensity measure, and non-destructive inspection. Normally, skilled workers move to the workspace by using transportation equipment such as a gondola and conduct the above tasks. However, it is ineffective in terms of time, cost, and safety. Also, putting a person directly into operations conducted in disaster recovery sites may cause a loss in life. Since those places are difficult to reach with the ground-based mobile robots, an *aerial manipulator* (Figure 1(b)), which combines the

maneuverability of an aerial vehicle and the versatility of a robotic arm, helps workers conduct such tasks autonomously.

Figure 2 (a) Skilled workers on the tall building (b) Rescue workers on the disaster recovery site.

Unmanned aerial manipulators (UAMs) interacting with structures located in hard-to-reach areas has been one of the most popular research topics in aerial robotics. Such tasks include window-cleaning[1], painting[2], and non-destructive inspection[3], and there needs a motion/force controller for operations with higher precision. Particularly, for the tasks such as teleoperation[4], multi-manual object manipulation[5] and plug-pulling[6], the capability to track the time-varying motion/force trajectories is also required. However, very few studies have designed a time-varying motion/force tracking controller which simultaneously considers model uncertainty and switching between the free and contact motion.

In the previous works[7~9], motion/force controllers for the omnidirectional aerial vehicles equipped with a robotic arm were proposed. However, since we are more interested in utilizing a conventional underactuated multirotor rather than developing a special configuration for an omnidirectional aerial vehicle, we focus on designing a motion/force controller for an underactuated UAM (uUAM) configured with an underactuated multirotor and a robotic arm.

An impedance-based force controller was presented for a uUAM conducting peg-in-hole insertion tasks [10, 11], and an image-based visual impedance force controller was introduced[12]. However, those controllers were designed under the assumption that the desired force is constant. Also, a contact force tracking controller minimizing the battery consumption was proposed[13], and a nonlinear motion/force model predictive controller was introduced[14]. However, they only conducted tracking experiments for constant force. Although the tracking of time-varying force was conducted[15~17], they did not prove the stability under the model uncertainty and switching behavior between the free and contact motion.

In this paper, we present a motion/force controller for a uUAM which guarantees both the tracking of time-varying motion/force trajectories and stability during the transition between the free and contact motions. To this end, we derive the translational dynamic model of the uUAM exerting force on a tilted surface with respect to the position of the end-effector, and model the force as the Kelvin-Voigt linear model. Also, a disturbance-observer (DOB)-based motion/force controller is designed, and its gains are calculated to satisfy the analytically obtained input-to-state stability conditions, considering the model uncertainty as well as the switching between the free and contact motions. To validate the proposed controller, we conduct time-varying force-tracking experiments on a tilted surface with a coaxial octocopter-based aerial manipulator with different approach speeds as shown in Figure 3.

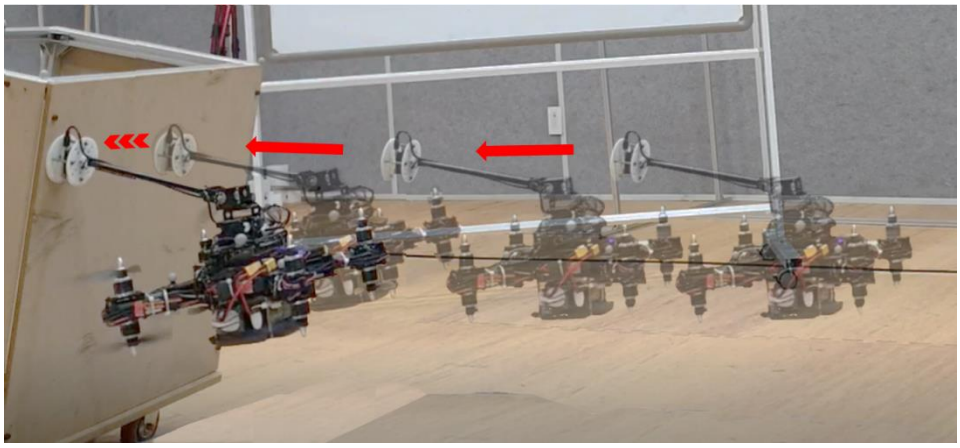

Figure 3 An aerial manipulator approaches a tilted surface and tracks the desired motion and force trajectories while maintaining stable contact.

This paper is outlined as follows; In the second section, we formulate the translational dynamic model of a uUAM exerting force to a tilted surface, and we describe the planning and control strategies for motion/force tracking in the third section. In the fourth section, we present a scheduling procedure of the controller gains which are utilized during the contact motion, and the proposed controller is validated experimentally in the fifth section.

Notations: 0_{ij}, I_i and e_3 represent the $\mathrm{i}\times\mathrm{j}$ zero matrix, $\mathrm{i}\times\mathrm{i}$ identity matrix and $[0;0;1]$, respectively. For vectors α and β, we let α_i and $[\alpha]_\times \in \mathbb{R}^{3\times3}$ denote the i-th element of α and the operator which maps α into a skew-symmetric matrix such as $[\alpha]_\times\beta = \alpha\times\beta$, respectively. Also, we abbreviate the phrase "with respect to" to w.r.t..

Translational Dynamic Model

Dynamic Equation w.r.t. the Position of the End-Effector

In Figure 4, coordinate frames to describe the configuration of the uUAM and the tilted surface are defined. Let O_I, O_b and O_e denote the inertial, multirotor body and end-effector coordinate frames, respectively, and O_s the surface coordinate frame with its x axis aligned with the force exerting direction. The generalized coordinate variables of the uUAM $q \triangleq [p;\phi;\theta]$ is defined with the position of the multirotor in O_I, $p \triangleq [p_x;p_y;p_z]$, the Euler angles of the multirotor, $\phi \triangleq [\phi_\mathrm{x};\phi_\mathrm{y};\phi_\mathrm{z}]$, and the joint angles of the robotic arm, $\theta \triangleq [\theta_1;\cdots;\theta_\mathrm{n}]$. We set the generalized control input τ as $[\mathrm{TR}(\phi)\mathrm{e}_3\ ;\tau_\phi\ ;\tau_\theta]$ where $\mathrm{T}\in\mathbb{R}$, $\mathrm{R}(\phi)\in\mathrm{SO}(3)$ $\tau_\phi\in\mathbb{R}^3$ and $\tau_\theta\in\mathbb{R}^{\mathrm{n_a}}$ represent the total thrust of the multirotor, the rotation matrix from $\mathrm{O_b}$ to $\mathrm{O_I}$, the body torque in the body frame and the actuator torques of the robotic manipulator, respectively, where $\mathrm{n_a}$ means the number of actuators used in the robotic arm.

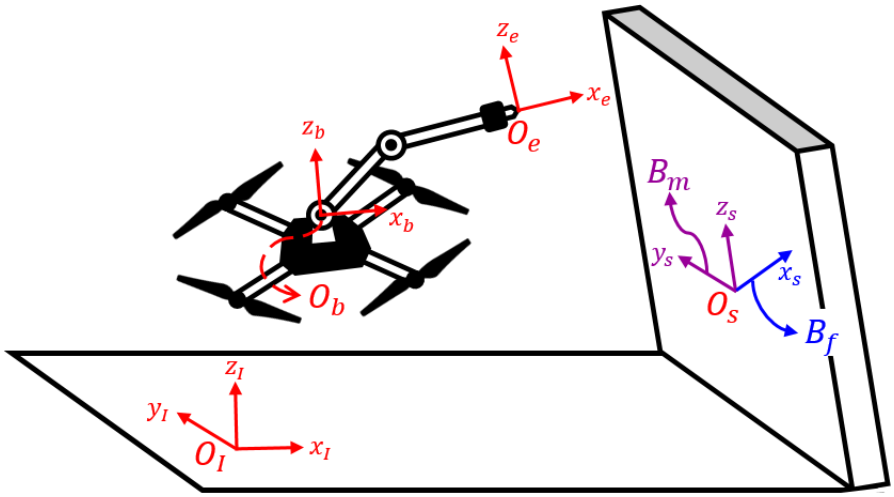

Figure 4 Illustration of a uUAM flying in front of a tilted surface. Coordinate frames required to demonstrate the uUAM system and the basis vectors of force and motion spaces are depicted.

According to the previous research[18], the translational dynamic model w.r.t. the center-of-mass position of a uUAM, $\mathrm{p_t}$, is expressed as follows:

$$\mathrm{m_t}\ddot{p}_t + \mathrm{m_t} g e_3 = TRe_3 + f_e + \delta_t \tag{1}$$

where $\mathrm{m_t}$, $\mathrm{g} \in \mathbb{R}$ and $\delta_t \in \mathbb{R}^3$ express the mass of the uUAM, gravitational acceleration and translational part of exogenous disturbance, respectively. To arrange (1) w.r.t. the position of the end-effector $\mathrm{p_e}$, we obtain the relation between $\mathrm{p_t}$ and $\mathrm{p_e}$ as follows:

$$\begin{aligned} p_t &= \frac{m}{m_t}p + \frac{m_e}{m_t}p_e + \sum_{i=1}^{n_o}\frac{m_i}{m_t}p_i = \frac{m}{m_t}\left(p_e - Rp_{be}(\theta)\right) + \frac{m_e}{m_t}p_e + \sum_{i=1}^{n_o}\frac{m_i}{m_t}\left(p_e - R(p_{be}(\theta) - p_{bi}(\theta))\right) \\ &= p_e - R\left(\frac{m_e}{m_t}p_{be}(\theta) + \sum_{i=1}^{n_o}\frac{m_i}{m_t}\left(p_{be}(\theta) - p_{bi}(\theta)\right)\right) \triangleq p_e - Rd(\theta) \end{aligned} \tag{2}$$

where m, $\mathrm{m_e}$ and $\mathrm{m_i}$ mean the mass of the multirotor, the end-effector and the i-th object of the robotic manipulator, respectively, and $\mathrm{n_o}$ represents the number of the added objects. Also, we let $\mathrm{p_{be}}(\theta)$ and $\mathrm{p_{bi}}(\theta)$ denote the positions of the end-effector and the i-th object w.r.t. $\mathrm{O_b}$, respectively. If we differentiate $\mathrm{p_t}$ twice w.r.t. time and substitute it for (1), the translational dynamic equation w.r.t. $\mathrm{p_e}$ is formulated as follows:

$$\mathrm{m_t}\ddot{p}_e = -m_t g e_3 + u_e + f_e + \Delta_e \tag{3}$$

where

$$\Delta_e \triangleq m_t R\left(([\omega_b]_\times^2 + [\omega_b]_\times)d + 2[\omega_b]_\times \dot{d} + \ddot{d}\right) + \delta_t,$$

$$\mathrm{u_e} \triangleq TRe_3 = T\Psi\Phi,$$

$$\Psi \triangleq \begin{bmatrix} c_{\phi_z} & s_{\phi_z} & 0 \\ s_{\phi_z} & -c_{\phi_z} & 0 \\ 0 & 0 & 1 \end{bmatrix},\ \Phi \triangleq \begin{bmatrix} c_{\phi_x}s_{\phi_y} \\ s_{\phi_x} \\ c_{\phi_x}c_{\phi_y} \end{bmatrix}$$

with angular velocity of O_b w.r.t. O_I expressed in O_b, ω_b.

Control Input Extraction

In (3), u_e acts as a control input. However, since the roll and pitch angles cannot be manually set, there needs the following assumption on the relation between $(\phi_x(t), \phi_y(t))$ and its reference trajectory $(\phi_{x,r}(t), \phi_{x,r}(t))$ as follows:

Assumption 1: Attitude controller is properly designed so that the roll and pitch angles $\phi_x(t)$ and $\phi_y(t)$ follow their reference trajectories $\phi_{x,r}(t)$ and $\phi_{y,r}(t)$ as follows:

$$\phi_x(t) = \phi_{x,r}(t - \gamma_{\phi_x}),\ \phi_y(t) = \phi_{y,r}(t - \gamma_{\phi_y}) \tag{4}$$

with time-varying nonnegative delays γ_{ϕ_x} and γ_{ϕ_y}.

According to [19], if we simply replace $(\phi_x(t), \phi_y(t))$ in u_e into $(\phi_{x,r}(t), \phi_{y,r}(t))$, respectively, there might be control performance degradation due to the error in roll and pitch angles. If we let $\bar{u}_e$ denote the desired value of u_e calculated by a well-designed position controller, we extract the desired roll, pitch angles and total thrust ($\bar{T}$) as follows:

$$\bar{T} = \frac{\Psi \bar{u}_{e,3}}{c_{\phi_x} c_{\phi_y}},\ \phi_{x,r} = \sin^{-1}\left(\frac{\Psi \bar{u}_{e,2}}{\bar{T}}\right),\ \phi_{y,r} = \sin^{-1}\left(\frac{\Psi \bar{u}_{e,1}}{\bar{T} c_{\phi_x}}\right) \tag{5}$$

Dynamic Equation Decomposition

To conduct motion/force control, the translational dynamic model (3) is decomposed into two parts, force and motion, as introduced in [20]:

$$\mathrm{m_t}\ddot{x}_f = -\mathrm{m_t} g B_f^{\mathrm{T}} e_3 + u_f + f_f + B_f^{\mathrm{T}} \Delta_e \tag{6}$$

$$\mathrm{m_t}\ddot{x}_m = -\mathrm{m_t} g B_m^{\mathrm{T}} e_3 + u_m + f_m + B_m^{\mathrm{T}} \Delta_e \tag{7}$$

where $x_f \triangleq B_f^{\mathrm{T}} p_e$, $u_f \triangleq B_f^{\mathrm{T}} u_e$, $f_f \triangleq B_f^{\mathrm{T}} f_e$, $x_m \triangleq B_m^{\mathrm{T}} p_e$, $u_m \triangleq B_m^{\mathrm{T}} u_e$ and $f_m \triangleq B_m^{\mathrm{T}} f_e$ with the basis vector of the force part, $\mathrm{B_f} \in \mathbb{R}^3$, and the concatenation of the basis vectors of the motion part, $B_m \in \mathbb{R}^{3\times 2}$. In (6), the force exerted to the end-effector that is normal to the tilted surface, f_f, is expressed with the following Kelvin-Voigt linear model:

$$f_f = -k_e\left(x_f - x_{f,s}\right) - b_e \dot{x}_f \tag{8}$$

where $x_{f,s} \triangleq B_f^{\mathrm{T}} p_s$ where $k_e, b_e \in \mathbb{R}$ and $p_s \in \mathbb{R}^3$ represent the environment stiffness, environment damping coefficient and the position of the contact point w.r.t. $\mathrm{O_I}$, respectively. Meanwhile, the friction force tangential to the surface, f_m, is treated as an exogenous disturbance. Hence, because $\mathrm{B_f}$ and B_m are orthonormal to each other as shown in Figure 4, (6) and (7) are rearranged as follows:

$$m_t \ddot{x}_f = -m_t g B_f^{\mathrm{T}} e_3 + \bar{u}_f + f_f + \Delta_f \tag{9}$$

$$m_t \ddot{x}_m = -m_t g B_m^{\mathrm{T}} e_3 + \bar{u}_m + \Delta_m \tag{10}$$

where $\bar{u}_f \triangleq B_f^{\mathrm{T}} \bar{u}_e$, $\bar{u}_m \triangleq B_m^{\mathrm{T}} \bar{u}_e$, $\Delta_f \triangleq \bar{u}_f - u_f + B_f^{\mathrm{T}} \Delta_e$ and $\Delta_m \triangleq \bar{u}_m - u_m + f_m + B_m^{\mathrm{T}} \Delta_e$.

Controller Design

In this section, the structure of the motion/force controller is presented. To this end, we first estimate k_e and b_e in (8) using recursive least-squares estimation (RLSE). Then, we generate the reference trajectories of x_f, f_f and x_m and calculate the control inputs $\bar{u}_f$ and $\bar{u}_m$.

Environment Parameter Estimation

As introduced in [21], we estimate k_e and b_e as follows:

$$\begin{aligned} &\epsilon \triangleq f_f - Y\hat{\theta}_e, && \dot{\hat{\theta}}_e = PY^{\top}\epsilon \\ &\dot{P} = \begin{cases} \mu_1 P - \mu_2 PY^{\top}YP, & \lambda_{\max}(P) \le \rho_M \\ 0_{21}, & \text{otherwise} \end{cases} \end{aligned} \tag{11}$$

where $\mathrm{Y} \triangleq -\left[x_f - B_f^{\top}p_s \;\; \dot{x}_f\right]$, $\hat{\theta}_e \triangleq \left[\hat{k}_e; \hat{b}_e\right]$ and $\lambda_{\max}(\cdot)$ represents the maximum eigenvalue of a square matrix with a large positive number ρ_{M}. Since the undesirable peaking in $\hat{\theta}_e$ can hinder the generation of reference motion/force trajectories, we set its lower and upper bounds as $\hat{k}_e \in \left[k_{e,m}, k_{e,M}\right]$ and $\hat{b}_e \in \left[b_{e,m}, b_{e,M}\right]$.

Reference Motion/Force Trajectories Generation

To enhance the control performance, we generate smooth reference trajectories of motion and force $x_{f,r}(t)$, $x_{m,r}(t)$ and $f_{f,r}(t)$ from their setpoints $x_{f,d}(t)$, $x_{m,d}(t)$ and $f_{f,d}(t)$ [22]. When the uUAM is flying in the free space, the reference trajectories are generated as follows:

$$\ddot{x}_{f,r} = -2\omega_n\dot{x}_{f,r} - \omega_n^2\left(x_{f,r} - x_{f,d}\right), \qquad f_{f,r} = 0, \qquad \ddot{x}_{m,r} = -2\omega_n\dot{x}_{m,r} - \omega_n^2(x_{m,r} - x_{m,d}) \tag{12}$$

with a natural frequency ω_n. Meanwhile, when the uUAM is in the contact motion, the reference trajectories are generated as follows:

$$\ddot{x}_{f,r} = -\frac{\hat{k}_e}{\hat{b}_e}\dot{x}_{f,r} - \frac{1}{\hat{b}_e}\dot{f}_{f,r}, \quad \ddot{f}_{f,r} = -2\omega_n\dot{f}_{f,r} - \omega_n^2(f_{f,r} - f_{f,d}), \quad \ddot{x}_{m,r} = -2\omega_n\dot{x}_{m,r} - \omega_n^2(x_{m,r} - x_{m,d}). \tag{13}$$

DOB-based Motion/Force Controller

Let $\bar{m}_t$ and $\bar{g}$ denote the nominal values of m_t and g, respectively, the switching control laws for $\bar{u}_m$ and $\bar{u}_f$ are shown as follows:

$$\begin{aligned} \bar{u}_f &= \begin{cases} \bar{m}_t\ddot{x}_{f,r} + k_d\dot{e}_{x,f} + k_p e_{x,f} + \bar{m}_t\bar{g}B_f^{\top}e_3 - \hat{\Delta}_f, & (\text{free motion}) \\ \bar{m}_t\ddot{x}_{f,r} - f_{f,r} - k_f e_{f,f} + b_f\dot{e}_{x,f} + \bar{m}_t\bar{g}B_f^{\top}e_3 - \hat{\Delta}_f, & (\text{contact motion}) \end{cases} \\ \bar{u}_m &= \bar{m}_t\ddot{x}_{m,r} + K_{m,d}\dot{e}_{x,m} + K_{m,p}e_{x,m} + \bar{m}_t\bar{g}B_m^{\top}e_3 - \hat{\Delta}_m \end{aligned} \tag{14}$$

where $\mathrm{e}_{x,f} \triangleq x_{f,r} - x_f$, $\mathrm{e}_{x,m} \triangleq x_{m,r} - x_m$ and $\mathrm{e}_{f,m} \triangleq f_{f,r} - f_f$ with the user-defined positive parameters k_p, k_d and positive definite matrices $K_{m,p}$, $K_{m,p} \in \mathbb{R}^{2\times 2}$. Also, $\hat{\Delta}_f$ and $\hat{\Delta}_m$ are the estimated disturbances from the DOBs w.r.t. the force and motion spaces, and k_f and b_f are the **force-controller gains** calculated from the **force-controller-gain scheduler** which will be explained in the next section.

$\hat{\Delta}_f$ and $\hat{\Delta}_m$ are obtained from the DOBs formulated as follows:

$$\nu_f = \bar{m}_t L_f\dot{x}_f, \;\; \hat{\Delta}_f = z_f + \nu_f, \;\; \dot{z}_f = -L_f z_f + L_f\left(\bar{m}_t\bar{g}B_f^{\top}e_3 - f_f\bar{u}_f - \nu_f\right) \tag{15}$$

$$\nu_m = \bar{m}_t L_m \dot{x}_m,\ \hat{\Delta}_m = z_m + \nu_m,\ \dot{z}_m = -L_m z_m + L_m(\bar{m}_t \bar{g} B_m^{\mathrm{T}} e_3 - f_m \bar{u}_m - \nu_m)$$

when $L_f \in \mathbb{R}$ and $L_m \in \mathbb{R}^{2\times 2}$ represent a positive parameter and a positive definite matrix, respectively. According to [23], if $\dot{\Delta}_f$ and $\dot{\Delta}_m$ are bounded, $||\hat{\Delta}_f - \Delta_f||$ and $||\hat{\Delta}_m - \Delta_m||$ exponentially converge to the balls with certain radius.

Force-Controller-Gain Scheduler

In this section, we first derive the input-to-state stability conditions for the force-controller gains. Then, with given k_p, k_d, $\hat{k}_e$ and $\hat{b}_e$, we set k_f and b_f to the values located at the farthest point from the boundary that distinguishes when the given switched system is stable and unstable.

Input-to-State (ISS) Conditions

By substituting (8) and (14) for (9), the perturbed switched system is obtained as follows:

$$\dot{z}_f = A_i z_f + N w_i(t) = \begin{bmatrix} 0 & 1 \\ -K_i & -B_i \end{bmatrix} z_f + N w_i(t), \quad z_f \in \Omega_i(t), \quad i \in \{1,2\} \tag{16}$$

where $z_f \triangleq [e_{x,f}; \dot{e}_{x,f}]$, $N \triangleq [0;1]$,

$$\mathrm{K}_1 \triangleq \frac{k_p}{m_t}, \quad \mathrm{B}_1 \triangleq \frac{k_d}{m_t}, \quad \mathrm{K}_2 \triangleq \frac{(1+k_f)k_e}{m_t}, \quad \mathrm{B}_2 \triangleq \frac{(1+k_f)b_e + b_f}{m_t},$$

$$\Omega_1 \triangleq \{z_f \in \mathbb{R}^2 | x_{f,r} - z_{f,1} \le 0\}, \quad \Omega_2 \triangleq \{z_f \in \mathbb{R}^2 | 0 < x_{f,r} - z_{f,1}\},$$

$$w_1(t) \triangleq -\frac{\bar{m}_t \ddot{x}_{f,r} + (\bar{m}_t \bar{g} - m_t g) B_f^{\mathrm{T}} e_3 - \tilde{\Delta}_f}{m_t},\ w_2(t) \triangleq -\frac{\bar{m}_t \ddot{x}_{f,r} + (1+k_f)\left(\tilde{b}_e \dot{x}_{f,r} + \tilde{k}_e (x_{f,r} - x_{f,s})\right) + (\bar{m}_t \bar{g} - m_t g) B_f^{\mathrm{T}} e_3 - \tilde{\Delta}_f}{m_t}$$

with $\tilde{m}_t \triangleq \bar{m}_t - m_t$, $\tilde{k}_e \triangleq \hat{k}_e - k_e$, $\tilde{b}_e \triangleq \hat{b}_e - b_e$ and $\tilde{\Delta}_f \triangleq \hat{\Delta}_f - \Delta_f$.

According to [22], with $\Delta\mathrm{K} \triangleq \mathrm{K}_1 - \mathrm{K}_2$ and $\Delta\mathrm{B} \triangleq \mathrm{B}_1 - \mathrm{B}_2$, the solution of (16), $z_f(t)$, is ISS w.r.t. $w_i(t)$ if K_1, B_1, K_2 and B_2 satisfy at least one of the following conditions:

- **No switching conditions:** Stable transition from free to contact motion without detaching
  1. $\Delta\mathrm{B} < 0,\ 4\mathrm{K}_1 \le \mathrm{B}_1^2$ and $\frac{\Delta\mathrm{K}}{\Delta\mathrm{B}} < \frac{2\mathrm{K}_1}{B_1 - \sqrt{\mathrm{B}_1^2 - 4\mathrm{K}_1}}$
  2. $\Delta\mathrm{B} < 0,\ 4\mathrm{K}_2 \le B_2^2$ and $\frac{2\mathrm{K}_2}{B_2 + \sqrt{B_2^2 - 4K_2}} < \frac{\Delta K}{\Delta B}$
  3. $0 \le \Delta\mathrm{B}$ and $4\mathrm{K}_2 \le B_2^2$
- **Finite switching conditions:** Finite number of switches between free and contact motion before achieving the stable contact.
  1. $\Lambda_1 \Lambda_2 < 1$ where $\Lambda_\mathrm{i},\ \mathrm{i} \in \{1,2\}$,are defined as:
     i. If $\mathrm{B}_\mathrm{i}^2 < 4K_i$, $\Lambda_\mathrm{i} \triangleq \left(\frac{K_i}{\omega_i}\left(\frac{(\Delta K)^2}{L^2} + \frac{Q^2}{4\omega_i^2 L^2}\right)^{-\frac{1}{2}}\right)^{(-1)^i} e^{-\frac{B_i}{2\omega_i}\phi_i}$ with $\mathrm{L} \triangleq \sqrt{(\Delta K)^2 + (\Delta B)^2}$, $\phi_\mathrm{i} \triangleq$

$$\mathrm{mod}\left(-\tan^{-1}\left(\frac{(-1)^i 2\omega_i \Delta K}{Q}\right), -\pi\right),\ \omega_i \triangleq \frac{1}{2}\sqrt{4K_i - B_i^2} \text{ and } \mathrm{Q} \triangleq B_i\Delta\ K - 2K_i\Delta B$$

ii. If $\mathrm{B_i^2} = 4K_i$, $\Lambda_\mathrm{i} \triangleq \left|\frac{B_i L}{2\Delta K - B_i \Delta B}\right|$

iii. If $\mathrm{B_i^2} > 4K_i$, $\Lambda_\mathrm{i} \triangleq \left|\frac{\Delta K\lambda_{bi} + K_i\Delta B}{K_i L}\right|^{\frac{(-1)^i\lambda_{ai}}{\lambda_{bi}-\lambda_{ai}}} \left|\frac{\Delta K\lambda_{ai} + K_i\Delta B}{K_i L}\right|^{\frac{(-1)^i\lambda_{bi}}{\lambda_{ai}-\lambda_{bi}}}$ with $\lambda_\mathrm{ai} \triangleq \frac{-B_i - \sqrt{B_i^2 - 4K_i}}{2}$ and $\lambda_\mathrm{bi} \triangleq \frac{-B_i + \sqrt{B_i^2 - 4K_i}}{2}$.

If the above ISS conditions are satisfied, $z_f(t)$ is bounded to a small ball around the origin because $w_1(t)$ and $w_2(t)$ are also bounded due to the smoothness of reference trajectories $\mathrm{x}_{f,r}$, $\dot{\mathrm{x}}_{f,r}$ and $\ddot{\mathrm{x}}_{f,r}$.

Force-Controller-Gain Scheduler

Prior to calculating the force-controller gains, due to the motor saturation and the noise in velocity measurement, we need to set the limits of k_f and b_f as follows:

$$0 < k_{f,m} \le k_f \le k_{f,M}, \qquad 0 < b_{f,m} \le b_f \le b_{f,M} \tag{17}$$

With (17), the procedure of force-controller-gain scheduling is summarized as follows:

1. Find the convex hulls which envelop the *no switching conditions* 1, 2 and 3, respectively.
2. Find a convex hull with the largest area and set k_f and b_f to its center of geometry.
3. If all three convex hulls are empty sets, find k_f and b_f which minimize the cost function $J(k_f, b_f)$ defined as follows (related to the *finite switching condition*):

$$J(k_f, b_f) \triangleq \Lambda_1\Lambda_2 + \left(\frac{2}{k_{f,M} - k_{f,m}}\right)^2 \left(k_f - \frac{k_{f,M} + k_{f,m}}{2}\right)^2 + \left(\frac{2}{b_{f,M} - b_{f,m}}\right)^2 \left(b_f - \frac{b_{f,M} + b_{f,m}}{2}\right)^2 \tag{18}$$

4. If k_f and b_f do not exist, set k_f and b_f to $k_{f,m}$ and k_d, respectively.

To proceed with step 1), we need to find the region of force-controller gains which satisfy each of the *no-switching conditions*. The most straightforward way is to generate $(\mathrm{N}+1)^2$ grid points in the rectangular area represented by (17) and check whether the ISS conditions are satisfied as in Figure Figure 5. However, because the time complexity of this method is $\mathcal{O}(\mathrm{N}^2)$, the stable region of force-controller gains may not be obtained within a controller loop with large N Therefore, we rearrange the *no-switching conditions 1), 2) and 3)* into explicit inequalities, e.g., $f(k_f) \le b_f$, and find the grid points that comprise the convex hull of each condition. Figure 6 compares the computation time of the grid-based search algorithm and the method using the explicit inequalities, where the latter is much faster. Also, Figure 7 shows the comparative results of those two methods. Meanwhile, to proceed with step 3), we adopt the gradient-free optimization algorithms such as *pattern search*[24].

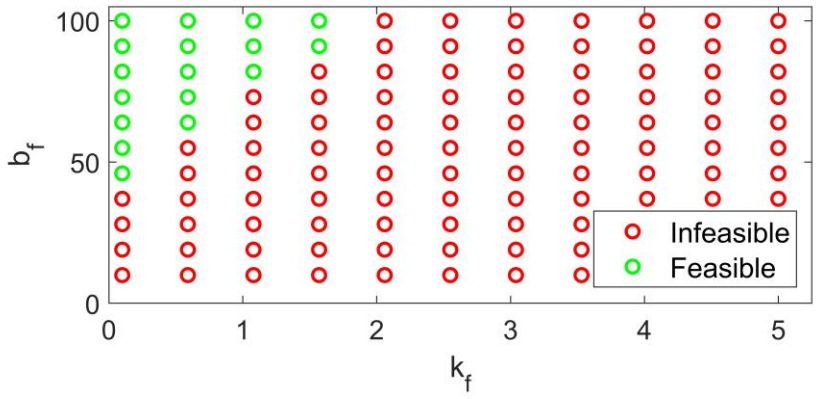

Figure 5 Example of grid-based search of stable region of force-controller gains (N = 20)

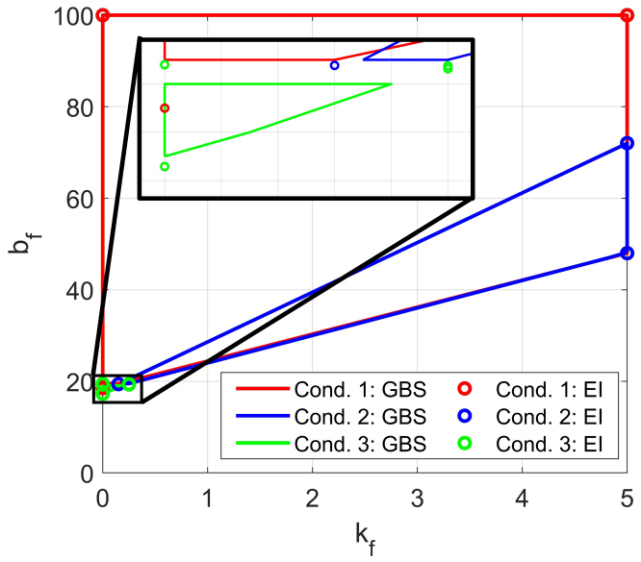

Figure 6 Computed results of region of stable force-controller gains by the grid-based search (GBS) and the method using explicit inequalities (EI)

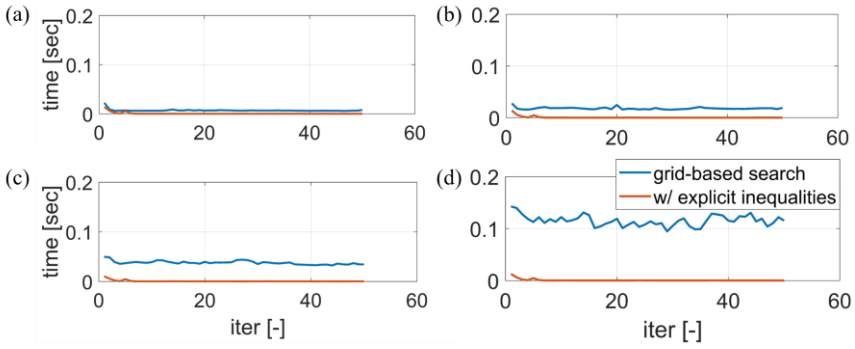

Figure 7 Comparison of computation time for searching stable regions of the force-controller gains when N = 75, 100, 125 and 175.

No switching condition 1)

If the inequality $4m_t k_p \le k_d^2$ holds, the other conditions are rearranged as follows:

$$\begin{gathered} -b_e(k_f+1)+k_d < b_f \\ \left(k_e\frac{k_d-\sqrt{k_d^2-4m_tk_p}}{2k_p}-b_e\right)k_f+(k_e-k_p)\frac{k_d-\sqrt{k_d^2-4m_tk_p}}{2k_p}+k_d-b_e<b_f. \end{gathered} \tag{19}$$

No switching condition 2)

The first and second inequalities are rearranged as follows:

$$\begin{gathered} -b_e(k_f+1)+k_d < b_f \\ -b_e(k_f+1)+2\sqrt{m_tk_e(1+k_f)} \le b_f. \end{gathered} \tag{20}$$

Meanwhile, the third equation is rearranged as follows:

$$(K_1+K_2)B_2-2B_1K_2<(K_2-K_1)\sqrt{B_2^2-4K_2} \tag{21}$$

To arrange this inequality in an explicit form, we first need to determine the sign of the left side of (21). If the left side is negative, the above inequality holds, otherwise, we obtain additional conditions by squaring the both sides. After a few computations, the additional condition is arranged as follows:

$$C_uk_p+(C_lk_e-b_e)(1+k_f)<b_f<C_lk_p+(C_uk_e-b_e)(1+k_f) \tag{22}$$

where $C_l \triangleq \frac{B_1-\sqrt{B_1^2-4K_1}}{2K_1}$ and $C_u \triangleq \frac{B_1+\sqrt{B_1^2-4K_1}}{2K_1}$ when $4m_tk_p \le k_d^2$ holds.

No switching condition 3)

This condition is rearranged in the form of explicit inequalities as follows:

$$-b_e(1+k_f)+2\sqrt{m_tk_e(1+k_f)} \le b_f \le -b_e(1+k_f)+k_d \tag{23}$$

Finite switching condition

Figure 8 shows that $\Lambda_1\Lambda_2$ has a bowl shape w.r.t. k_f and b_f. Thus, we can find a globally optimal point of (k_f, b_f) which minimizes $J(k_f, b_f)$ defined in step 3) using convex optimization. However, since we cannot differentiate $\Lambda_1\Lambda_2$ due to the modular expression, we need to utilize gradient-free algorithms. Since the given system gets more stable when $\Lambda_1\Lambda_2$ gets smaller and (k_f, b_f) gets further from their limits $[k_{f,m}, k_{f,M}]$ and $[b_{f,m}, b_{f,M}]$, we set k_f and b_f to the values which minimize the convex cost function $J(k_f, b_f)$ defined in (18) by using the *pattern search* algorithm.

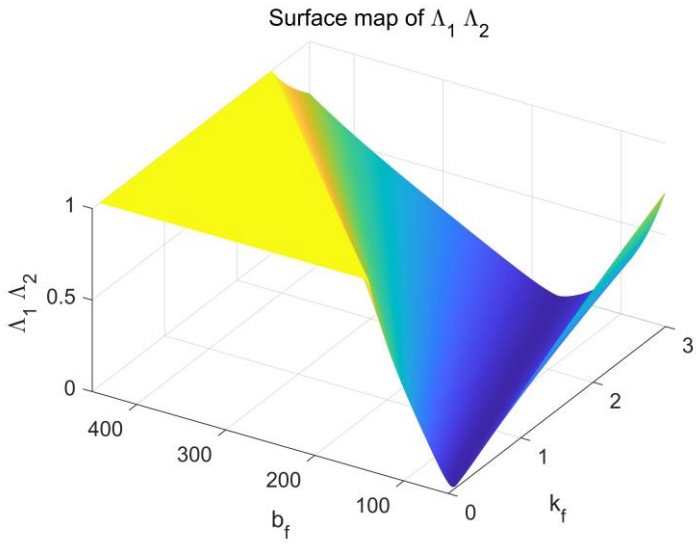

Figure 8 3D surface map of $\boldsymbol{\Lambda_1\Lambda_2}$

Experimental Results

This section reports the experimental validation of the proposed motion/force control strategy.

Experimental Setups

The experimental setup for this research consists of four parts: an underactuated coaxial octocopter, a robotic arm, a 1-axis force sensor and a tilted surface. The coaxial octocopter which weighs 3.78 kg was assembled with the custom-built frame, eight KDE2314XF-965 motors with corresponding KDEXF-UAS35 electronic speed controllers, and 9-inch APC LPB09045MR propellers, two Turnigy LiPo batteries for power supplement, and Intel NUC for computing. On Intel NUC, Robot Operating System (ROS) is installed in Ubuntu 18.04, and the position controller for the octocopter, servo-angle controller for the robotic arm and the navigation algorithm with Optitrack are executed. The attitude controllers are executed in Pixhawk 4 which is connected to the Intel NUC. The robotic arm is comprised of ROBOTIS dynamixel XH540 and XM430 servo motors. We mount Honeywell FSS2000NSB 1-axis force sensor to the end-effector which is connected to the arduino nano board. The tilted surface is made of medium density fibreboard (MDF) and we attach four Optitrack markers to that surface to measure its rotation matrix $[\mathrm{B_f}\ \mathrm{B_m}]$.

The values of the parameters during the experiments are arranged in Table 1.

Table 1 Parameters used in the experiments.

Estimation of Kelvin-Voigt linear model's parameters						
μ_1	μ_2	ρ_M	$k_{e,m}$	$b_{e,m}$	$k_{e,M}$	$b_{e,M}$
0.9996	0.9996	5000	50	0.1	500	1
Reference trajectory generation and controller						
ω_n	k_p	k_d	$K_{m,p}$	$K_{m,d}$		
10.0	23.5	19.5	$23.5I_2$	$19.5I_2$		

Force-controller-gain scheduler						
$k_{f,m}$	$b_{f,m}$	$k_{f,M}$	$b_{f,M}$			
0.1	10	1	40			

We assumed that only the orientation of the contact surface is known while its position is not given. Also, for the constant reference force, $\mathrm{f_{f,r}(t)}$ was set to −6 while it was set to $-3.5 + 2.5\cos\frac{2\pi t}{5}$ for the time-varying reference force.

Experiment 1: Force Tracking on the Tilted Surface with Two Different Approach Speeds

Scenario

The uUAM configured with an underactuated coaxial octocopter and a robotic arm approaches the tilted surface with two different approach speeds (0.1 m/s and 0.3 m/s) and exerts the constant or time-varying force onto a specific point of that surface.

Results

Figure 9a presents the measured values of position and exerted force of the end-effector, the force-controller gains and the estimated environment parameters when the uUAM attempts to exert the constant force to the tilted surface after approaching with the slow speed. As observed in the measured force values, the uUAM was able to track the constant reference force trajectory while keeping the constant position of the end-effector.

Meanwhile, we can also confirm that the proposed force-controller-gain scheduler successfully generated k_f and b_f along with the estimated values of k_e and b_e both in Figure 9a and Figure 9b.

Experiment 2: Force Tracking while Sliding on the Vertical and Tilted Surfaces

Scenario

In this experiment, the uUAM slides on a vertical or tilted surface while exerting the time-varying force for 20 seconds. The approach speed to the vertical surface is set to 0.3 m/s while that to the tilted surface is set to 0.1 m/s.

Results

The result of tracking the time-varying reference force trajectory while sliding on the vertical surface is shown in Figure 9c. The result of $x_{m,1}$ shows that the uUAM successfully slid in the $+y$ direction of the vertical surface while f_f followed $f_{f,r}$ after the initial oscillation. This result demonstrates that the proposed controller can make the uUAM simultaneously track the time-varying reference motion and force trajectories even with the high approach speed.

Figure 9d presents the result of tracking the time-varying force while sliding on the tilted surface. The force tracking performance is enhanced than Figure 9c due to the lower speed.

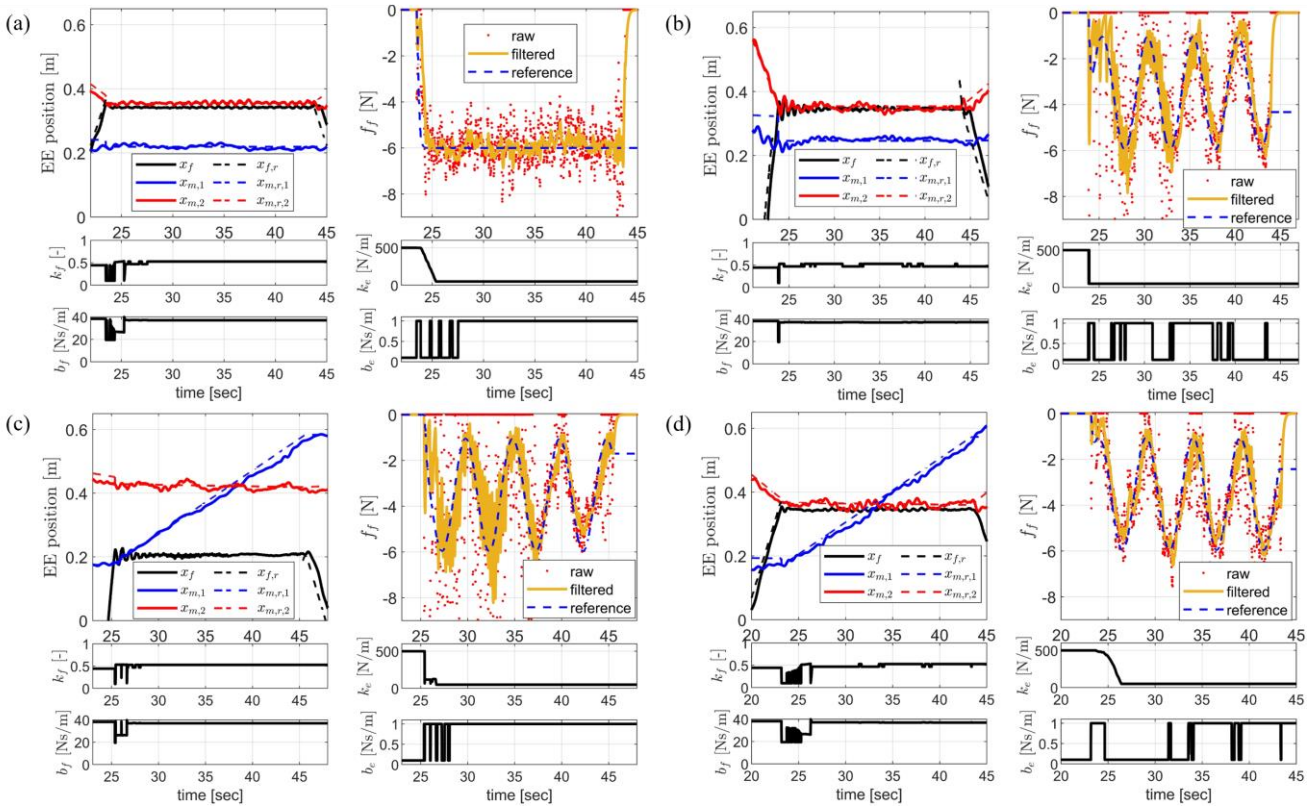

Figure 9 Histories of the end-effector's position ($\boldsymbol{p_e}$), force exerted on the end-effector ($\boldsymbol{f_f}$), force-controller gains ($\boldsymbol{k_f}$ and $\boldsymbol{b_f}$) and estimated environmental parameters ($\widehat{\boldsymbol{k}}_{\boldsymbol{e}}$ and $\boldsymbol{b_e}$) of (a) the first one of *Experiment 1*, (b) the second one of *Experiment 1*, (c) the first one of *Experiment 2* and (d) the second one of *Experiment 2*.

Conclusions

This paper presents motion/force control that guarantees a stable contact for an aerial manipulator on an arbitrarily tilted surface. To analyze the dynamic characteristics, the translational dynamic equation w.r.t. the position of the end-effector is derived, and decomposed into force and motion spaces where the force exerted on the end-effector is modeled as the Kelvin-Voigt linear model. Then, we estimate the parameters of Kelvin-Voigt linear model by recursive least-squares estimation, and generate the reference motion and force trajectories based on their setpoints. The disturbance-observer-based controller with scheduling of the force-controller gains is designed based on the stability conditions considering both model uncertainty and switching behavior between the free and contact motion. To check the performance of our controller, we conduct four different force tracking experiments with different approach speeds and reference motion/force trajectories. The results confirm that the proposed controller enables the aerial manipulator to simultaneously track the time-varying reference motion and force trajectories while maintaining stable contact. Future works may involve the design of a switching rule which can enhance the stability during the switch between the free and contact motion or a motion/force control law to push a movable structure.

References

[1] Y. Sun, Z. Jing, P. Dong, J. Huang, W. Chen, and H. Leung, “A switchable unmanned aerial manipulator system for window-cleaning robot installation,” IEEE Robotics and Automation Letters, vol. 6, no. 2, pp. 3483–3490, 2021.

[2] M. Orsag, C. M. Korpela, S. Bogdan, and P. Y. Oh, “Hybrid adaptive control for aerial manipulation,” Journal of intelligent & robotic systems, vol. 73, no. 1, pp. 693–707, 2014.

[3] M. Á. Trujillo, J. R. Martínez-de Dios, C. Martín, A. Viguria, and A. Ollero, “Novel aerial manipulator for accurate and robust industrial ndt contact inspection: A new tool for the oil and gas inspection industry,” Sensors, vol. 19, no. 6, p. 1305, 2019.

[4] M. Allenspach, N. Lawrance, M. Tognon, and R. Siegwart, “Towards 6dof bilateral teleoperation of an omnidirectional aerial vehicle for aerial physical interaction,” arXiv preprint arXiv:2203.03177, 2022.

[5] E. Shahriari, S. A. B. Birjandi, and S. Haddadin, “Passivity-based adaptive force-impedance control for modular multi-manual object manipulation,” IEEE Robotics and Automation Letters, vol. 7, no. 2, pp. 2194–2201, 2022.

[6] J. Byun, D. Lee, H. Seo, I. Jang, J. Choi, and H. J. Kim, “Stability and robustness analysis of plug-pulling using an aerial manipulator,” in 2021 IEEE/RSJ International Conference on Intelligent Robots and Systems (IROS). IEEE, 2021, pp. 4199–4206

[7] G. Nava, Q. Sablé, M. Tognon, D. Pucci, and A. Franchi, “Direct force feedback control and online multi-task optimization for aerial manipulators,” IEEE Robotics and Automation Letters, vol. 5, no. 2, pp. 331–338, 2019.

[8] K. Bodie, M. Brunner, M. Pantic, S. Walser, P. Pf ¨andler, U. Angst, R. Siegwart, and J. Nieto, “Active interaction force control for contact-based inspection with a fully actuated aerial vehicle,” IEEE Transactions on Robotics, vol. 37, no. 3, pp. 709–722, 2020.

[9] L. Peric, M. Brunner, K. Bodie, M. Tognon, and R. Siegwart, “Direct force and pose nmpc with multiple interaction modes for aerial push-and-slide operations,” in 2021 IEEE International Conference on Robotics and Automation (ICRA). IEEE, 2021, pp. 131–137.

[10] M. Car, A. Ivanović, M. Orsag, and S. Bogdan, “Impedance based force control for aerial robot peg-in-hole insertion tasks,” in 2018 IEEE/RSJ International Conference on Intelligent Robots and Systems (IROS). IEEE, 2018, pp. 6734–6739.

[11] L. Marković, M. Car, M. Orsag, and S. Bogdan, “Adaptive stiffness estimation impedance control for achieving sustained contact in aerial manipulation,” in 2021 IEEE international conference on robotics and automation (ICRA). IEEE, 2021, pp. 117–123.

[12] M. Xu, A. Hu, and H. Wang, “Image-based visual impedance force control for contact aerial manipulation,” IEEE Transactions on Automation Science and Engineering, 2022.

[13] T. Ikeda, S. Yasui, S. Minamiyama, K. Ohara, S. Ashizawa, A. Ichikawa, A. Okino, T. Oomichi, and T. Fukuda, “Stable impact and contact force control by uav for inspection of floor slab of bridge,” Advanced Robotics, vol. 32, no. 19, pp. 1061–1076, 2018.

[14] D. Tzoumanikas, F. Graule, Q. Yan, D. Shah, M. Popovic, and S. Leutenegger, “Aerial manipulation using hybrid force and position nmpc applied to aerial writing,” arXiv preprint arXiv:2006.02116, 2020.

[15] H. W. Wopereis, J. J. Hoekstra, T. H. Post, G. A. Folkertsma, S. Stramigioli, and M. Fumagalli, “Application of substantial and sustained force to vertical surfaces using a quadrotor,” in 2017 IEEE international conference on robotics and automation (ICRA). IEEE, 2017, pp. 2704–2709.

[16] C. Izaguirre-Espinosa, A.J. Muñoz-Vázquez, A. Sanchez-Orta, V. Parra-Vega, and P. Castillo, “Contact force tracking of quadrotors based on robust attitude control,” Control Engineering Practice, vol. 78, pp. 89–96, 2018.

[17] K. Yi, J. Han, X. Liang, and Y. He, “Contact transition control with acceleration feedback

enhancement for a quadrotor," ISA transactions, vol. 109, pp. 288–294, 2021.

[18] H. Yang and D. Lee, "Dynamics and control of quadrotor with robotic manipulator," in 2014 IEEE international conference on robotics and automation (ICRA). IEEE, 2014, pp. 5544–5549.

[19] S. J. Lee, S. H. Kim, and H. J. Kim, "Robust translational force control of multi-rotor uav for precise acceleration tracking," IEEE Transactions on Automation Science and Engineering, vol. 17, no. 2, pp. 562–573, 2019.

[20] J. Byun, H. J. Kim, and M. Kwon, "Hybrid motion/force control of the aerial manipulator without information on the added equipment," in Control Conference (ASCC), 2022 13th Asian. IEEE, 2022.

[21] Y. Lin, Z. Chen, and B. Yao, "Unified motion/force/impedance control for manipulators in unknown contact environments based on robust model-reaching approach," IEEE/ASME Transactions on Mechatronics, vol. 26, no. 4, pp. 1905–1913, 2021.

[22] D. Heck, A. Saccon, N. Van de Wouw, and H. Nijmeijer, "Guaranteeing stable tracking of hybrid position–force trajectories for a robot manipulator interacting with a stiff environment," Automatica, vol. 63, pp. 235–247, 2016.

[23] A. Mohammadi, M. Tavakoli, H. J. Marquez, and F. Hashemzadeh, "Nonlinear disturbance observer design for robotic manipulators," Control Engineering Practice, vol. 21, no. 3, pp. 253–267, 2013.

[24] C. Audet and J. E. Dennis Jr, "Analysis of generalized pattern searches," SIAM Journal on optimization, vol. 13, no. 3, pp. 889–903, 2002.